

# Surface radiant and energy flux densities inferred from satellite data for the BALTEX watershed

Franz H. Berger

*Technische Universität Dresden, Institute of Hydrology and Meteorology, Department of Meteorology, Piennnerstr. 9, D-01737 Tharandt, Germany*

Berger, F. H. 2002: Surface radiant and energy flux densities inferred from satellite data for the BALTEX watershed. — *Boreal Env. Res.* 7: 343–351. ISSN 1239-6095

To study the energy and water cycle at different spatial and temporal scales, the satellite data analysis scheme SESAT (Strahlungs- und Energieflüsse aus SATellitendaten) has been developed for passive remotely sensed data, like NOAA-AVHRR, ERS-1/2 ATSR, Envisat AATSR and MSG SEVIRI data. SESAT consists of several modules to compute cloud properties (types as well as geometrical, optical and microphysical properties), land surface properties (radiometrical and bio-geophysical properties), surface radiant and energy flux densities. SESAT could be applied to different data sets, especially for the BALTEX watershed, to infer surface radiant flux densities and also, as a first estimation, surface energy flux densities with sufficient accuracy. Most of the parameters needed for this computation can be derived from meteorological satellite data. Comparisons of net radiation, inferred from satellite data and measured at the surface, do show sufficient accuracy, but for energy flux densities more observations at the ground will have to be carried out to quantify the achievable accuracy.

## Introduction

To improve our knowledge of climate and weather prediction, related processes must be clearly understood and parameterised with different models. One goal is the investigation of the energy and water cycle at different scales, reaching from global to local scales with adequate temporal scales from months to seconds (Chahine 1992). The water cycle influences climate and weather in different ways. The exchange of energy and humidity between the Earth surface and the atmosphere influences dynamics

and thermodynamics in weather and climate regimes. Water in its different states plays a significant role in the heating or the cooling of the Earth/atmosphere system. A large fraction of the cooling of the Earth surface is due to evapotranspiration at the surface. The processes within the water and energy cycles are being studied in the context of large hydrological experiments, for example GEWEX (Global Energy and Water cycle EXperiment; WMO 1990) or BALTEX (Baltic Sea Experiment; Raschke 1994).

The dominant components of the energy and water cycle are clouds and radiation, atmospheric

humidity, precipitation, oceanic and land surface processes including storage and run-off (Chahine 1992). To study all these processes model simulations and various observations have to be merged. Thus, a large variety of observations is necessary, from local measurements at different field sites (routinely and/or experimentally) up to areal integrated remotely sensed measurements. However, remotely sensed data usually are instantaneous observations, hence the processes cannot be described. Nevertheless, process-related results may be derived from remotely sensed data, like a frontal zone or, more specifically, a convective cloud cell. Thus, the fluxes resulting from remotely sensed data are calculated as instantaneous values and, for the comparison with surface based measurements, either temporal or spatial averaged values are needed and considered (Berger 2001).

To study further small scale processes (both in space and time) with model simulations (Mason 1994, Moeng *et al.* 1996, Avissar and Schmidt 1998), which must include a detailed validation, different efforts have been made to determine areal integrated surface energy fluxes from point measurements and/or remotely sensed data (Moreno and Green 1996, Berger 1997, Mauser and Schädlich 1998). These studies have led to an enhanced knowledge of processes, though additional research will improve the quality. Thus, the aim of the present investigation has been the development and application of an analysis scheme to infer pixel-based surface radiant and energy fluxes from remotely sensed data for individual atmospheric conditions ranging from clear-sky to totally overcast. The satellite data analysis scheme SESAT (Strahlungs- und Energieflüsse aus SATellitendaten) was applied to different data sets, e.g. in May and June 1993 or in August and September 1995 for the BALTEX watershed.

## Radiant flux densities at surface

This section explains the structure of the satellite data analysis scheme SESAT to infer surface radiant and energy flux densities. The scheme has been developed for a variety of meteorologi-

cal, passive satellite data, like current NOAA-AVHRR, ERS-1/2 ATSR, Envisat AATSR and MSG SEVIRI data (Berger 2001). Future intentions are the processing of MSG data to allow a detailed analysis of the diurnal water and energy cycle and the study of processes within these cycles, utilizing the 15 minute time interval of MSG observations.

An overview of the modular analysis scheme SESAT is displayed in Fig. 1. An accurate calibration (Koslowksy 1997) and a detailed geocoding (Koslowksy 1977) is followed by a cloud classification (Berger 1992, Berger 1995). The cloud classification is based on the maximum-likelihood classifier discriminating 26 cloud classes for clouds at different levels with varying cloud optical depths. Moreover, panel B in Fig. 1 includes threshold techniques to distinguish clouds from snow and sunglint areas (Khattak *et al.* 1991, Derrien *et al.* 1993). The results are used to assume cloud properties, necessary for the following radiative transfer computations.

Panel C in Fig. 1 allows cloud properties to be inferred — the cloud optical depth as well as effective cloud droplet radius or effective ice crystal diameter — applying an inverse remote sensing technique. This technique is based on intensive radiative transfer simulations (Streamer; Key 1999) to produce sets of look-up tables. Consequently, a large variety of parameters is taken into account: different viewing conditions (solar zenith angle from 0° to 75° in steps of 5°, satellite viewing angle from 0° to 50° in 5° steps), various atmospheric properties (relative humidity from 0% to 100% in 5% steps and visibility within the atmospheric boundary layer from 1 to 50 km), different land surface properties (different landuse types like bare soil, vegetation, forest, sea, snow, and their related reflectances), and the classified cloud type. These look-up tables are interpolated to actual conditions. So, by using a single band in the visible (about 0.6  $\mu\text{m}$ ) the cloud optical depth can be inferred (Berger *et al.* 1995), whereas by using two bands (about 0.6  $\mu\text{m}$  and 1.6  $\mu\text{m}$ ) the effective droplet radius or the effective ice particle diameter can additionally be determined (Nakajima and King 1990). Nevertheless, it is obvious that an accurate determination of cloud optical depth, especially between

0.5 and 30, is more significant for the computation of surface radiant and energy fluxes than the determination of cloud microphysical properties (Berger 2001). Another important aspect for the computing of surface fluxes is the influence of the three-dimensional cloud field structure, which is not considered within this study. Using the cloud top temperatures, cloud top heights could further be estimated assuming a standard atmospheric profile.

Within panel D in Fig. 1, land surface properties required for the determination of surface flux densities will be derived. The surface reflectance is inferred applying a 7-days sampling including an atmospheric correction after Vermote *et al.* (1995). Furthermore bio-geophysical properties, like the leaf area index LAI or the roughness length, are calculated using relations mainly based on NDVI (normalized difference vegetation index) results (Gao *et al.* 1998).

After the computation of TOA (top of atmosphere) radiant fluxes (panel E in Fig. 1), using a narrow-to-broadband conversion scheme, the surface radiant flux densities are determined again through an inverse remote sensing technique. In this panel, additional properties, mainly the cloud properties from panel F in Fig. 1, are considered. As far as the TOA fluxes are concerned, the narrow-to-broadband conversion considers the filter response functions and the radiant intensities within the solar and terrestrial spectrum of all available channels as well as the surface conditions. All radiative flux components including ultra-violet (UV) flux densities can be calculated (Podlasly and Berger 2001). A digital elevation model (USGS GTOPO30) is considered to compute altitude dependent flux densities. To determine longwave fluxes at surface, look-up tables are also applied, where in case of cloudy pixels the flux densities are modified depending on cloud optical depth, cloud base height and cloud type (Mecklenburg *et al.* 1999). The cloud base heights which cannot be inferred from passive remotely sensed data are assumed from climatological information considering the classified cloud type. Adding all radiant flux components, the net radiation at surface is calculated, representing the most relevant quantity for the energy balance at surface.

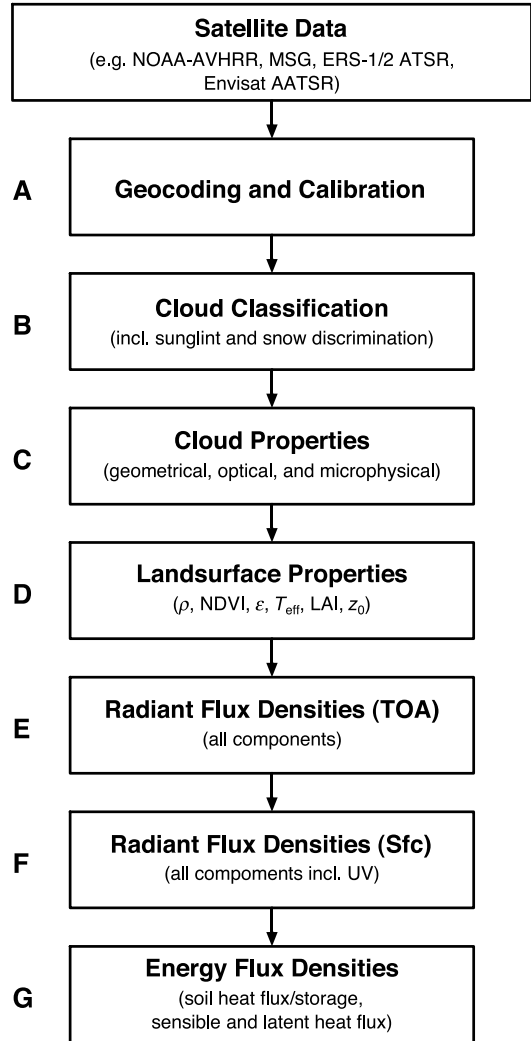


Fig. 1. Satellite data analysis scheme SESAT.

## Energy flux densities inferred from satellite data

Within panel G in Fig. 1, the energy flux densities, as a first estimate based on climatological conditions, can be calculated as follows:

$$M^* = M_S + M_{LH} + M_{SH} \quad (1)$$

The first component is the soil heat flux  $M_S$ , which for high vegetation also includes the storage within the canopy. Empirical equations used for the soil heat flux are mainly based on rela-

tions between net radiation and NDVI for different vegetation types (Gao *et al.* 1998, Schwiebus and Podlasly 2001), which vary depending on net solar radiation. For forest a simple relation was found (Berger 2001), where only small flux densities are computed (up to  $35 \text{ W m}^{-2}$  for both the soil heat flux and the storage within the canopy).

To compute the latent heat flux density  $M_{\text{LH}}$ , three different approaches are available within SESAT. All approaches have been developed for climatological studies, but will be used in this study as a first estimate for instantaneous observations, because ground measured flux densities differ due to varying atmospheric conditions. The approach after Priestly-Taylor (1972) allows the determination of the potential evaporation:

$$M_{\text{LH,PT}} = 1.26 \frac{s}{s + \gamma} (M^* - M_s) \quad (2)$$

The latent heat flux density  $M_{\text{LH,PT}}$  depends mainly on the available energy ( $M^* - M_s$ );  $s$  is the slope of saturation water vapour pressure and  $\gamma$  the psychrometer constant.

Replacing the qualitative and poorly defined potential evaporation, the grass-reference evaporation was defined as an international standard by FAO (DVWK 1996). This quantitative reference evaporation shows the evapotranspiration of a saturated grass surface for a given location and can therefore be used as a calibration:

$$M_{\text{LH,g}} = \frac{s}{s + \gamma^*} (M^* - M_s) + \frac{\gamma}{s - \gamma^*} \frac{3.75}{t_{2m} + 273} Lu_{2m} [e_s(t_{2m}) - e(t_{2m})] \quad (3)$$

where  $\gamma = 1 + 0.34u_{2m}$  and the latent heat of water vaporization  $L = 28.9 - 0.28(T - 273)$ . Equation 3 shows a more complex relation, where the humidity (water vapour pressure  $e$ ) within the boundary layer and the wind speed  $u_{2m}$  are considered additionally. The 2m-temperature is computed after de Rooy and Holtslag (1999):

$$t_{2m} - t_s = \frac{M_s}{A_G}, \quad (4)$$

where  $A_G$  is a fixed value for grass of  $9 \text{ W m}^{-2} \text{ K}^{-1}$ . It has to be taken into account that net radiation and soil heat flux can be inferred from remotely

sensed data as a function of NDVI, whereas the atmospheric humidity and the wind speed can only be measured at ground. Therefore, the present study assumes a fixed relative humidity of 55% and a fixed wind speed of  $3 \text{ m s}^{-1}$ .

Another relation used in SESAT is the relationship after Penman-Monteith (Monteith 1965):

$$M_{\text{LH,PM}} = \frac{s}{s + \gamma \left(1 + \frac{r_c}{r_a}\right)} (M^* - M_s) + \frac{1}{s + \gamma \left(1 + \frac{r_c}{r_a}\right)} \frac{\rho c_p}{r_a} \times [e_s(t_{2m}) - e(t_{2m})] \quad (5)$$

The resistances in Eq. 5 can be computed for different landuse classes. The landuse classes are based on the USGS landuse classification scheme. Thus, the canopy resistance can be determined after Maidment (1993):

$$r_c = \frac{200}{\text{LAI}} \quad (6)$$

The aerodynamical resistance after Gao *et al.* (1998) is computed as follows:

$$r_a = \frac{0.74}{\kappa^2 u_{2m}} \left[ \ln \frac{z-d}{d} \right]^2 \quad (7)$$

considering  $d = 2/3 h_0$  (Brutsaert 1988). The height of specific vegetation areas  $h_0$  is computed using the roughness length  $z_0$ : for grass  $h_0 = 7.35z_0$ , for forest  $h_0 = 13.2z_0$  and for urban areas  $h_0 = 11.2z_0$  (Wierenga 1993). For low vegetation ( $z_0 < 7 \text{ cm}$ ), the roughness length was computed after Gao *et al.* (1998):

$$z_0 = 2.0 \times 10^{(-4.3 + 2.875\text{NDVI})}, \quad (8)$$

where NDVI is the normalised difference vegetation index  $\text{NDVI} = (\rho_{\text{NIR}} - \rho_{\text{VIS}}) / (\rho_{\text{NIR}} + \rho_{\text{VIS}})$ , applying the relevant NOAA-AVHRR channels. All other information especially for other landuse classes, which are needed in Eq. 5, are taken from comparable model assumptions (Hagemann 1999). To compute canopy resistance after Eq. 6, the leaf area index (LAI) is needed. This parameter may be inferred from passive remotely sensed data for different vegetation types, for example

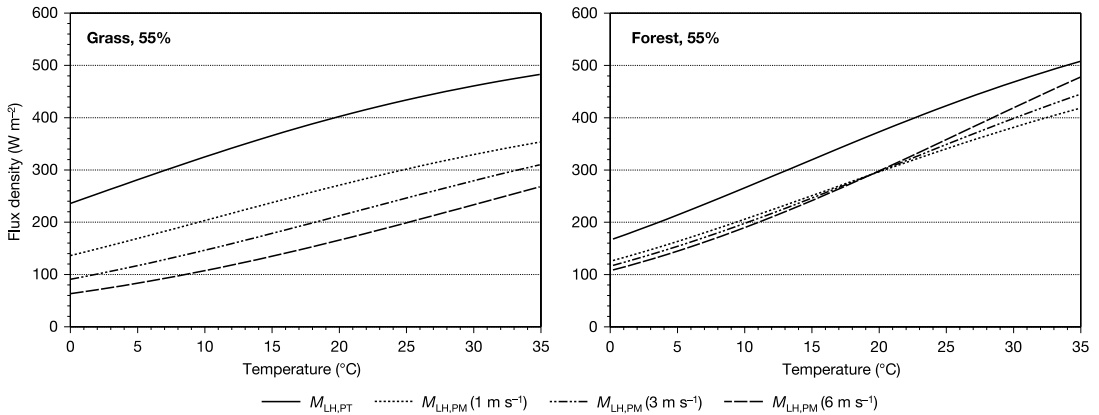


**Fig. 2.** Evaporation for grass (left panel) and for forest (right panel) after Priestley-Taylor and Penman-Monteith for three different wind speeds and constant relative humidity.

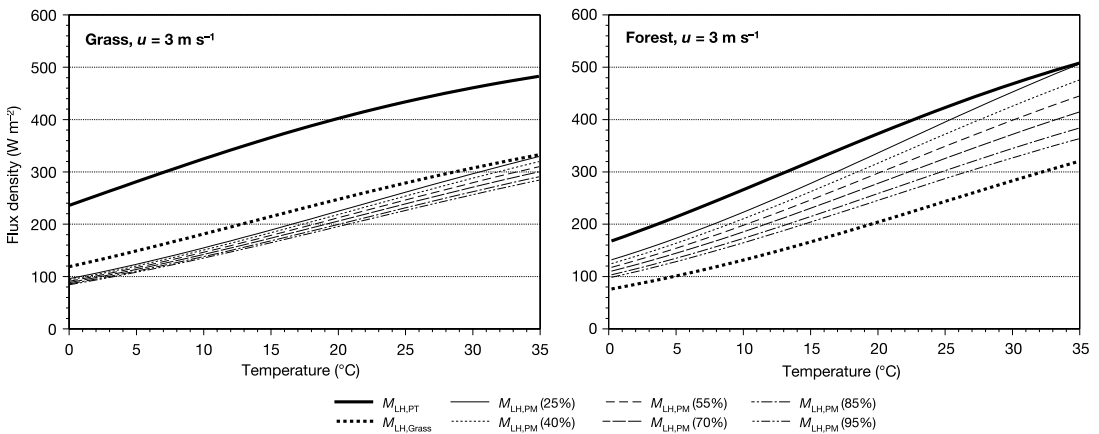


**Fig. 3.** Evaporation for grass (left panel) and for forest (right panel) after Priestley-Taylor, after Penman-Monteith as well as the grass-reference evaporation for different relative humidities and fixed wind speed.

for coniferous forest after Running and Nemani (1989), for deciduos forest after BAHC (1993), and for grass after Friedl (1996).

Figure 2 shows simulated evaporation rates for grass and forest based on a net radiation of  $600 \text{ W m}^{-2}$  after Priestley-Taylor and Penman-Monteith for three different wind speeds and constant relative humidity. In both cases the Priestley-Taylor evaporation results in the highest evaporation rate (potential evaporation). After Penman-Monteith the evapotranspiration is reduced and decreases with increasing wind speeds. These differences are much larger for grass than for forest. Assuming a constant wind speed of  $3 \text{ m s}^{-1}$  the error in evaporation for grass is in the order of  $\pm 50 \text{ W m}^{-2}$ , while it is negligible for forest. Similar evaporation

rates but with fixed wind speed and varying relative humidities are shown in Fig. 3. Here the evaporation is more or less independent of relative humidity for grass surfaces, but depends strongly on it for forest. By varying the relative humidity the differences between the resulting grass-reference evaporation are very small. Again, there is a slight uncertainty of  $\pm 50 \text{ W m}^{-2}$  in the determination of evaporation, but only for the forest. So, for both vegetation types the uncertainty in the determination of actual evaporation is about  $\pm 50 \text{ W m}^{-2}$ .

Finally, the sensible heat flux density  $M_{SH}$  is computed as the residuum of all inferred components and depends therefore on their accuracy. The difference to a direct estimate of sensible heat flux densities determined by using the 2m-

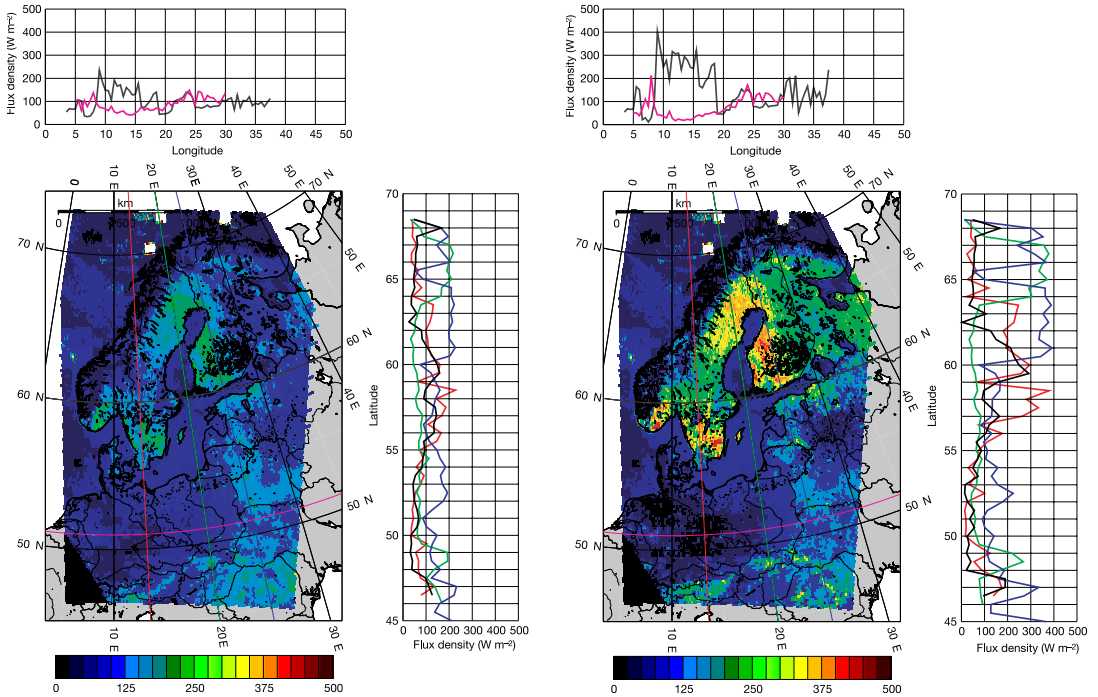


**Fig. 4.** Grass-reference evaporation (left panel) and evapotranspiration after Penman-Monteith (right panel) for 15 June 1993 13:15 UTC.

and the surface temperatures for specific landuse types gives an indication about the achievable accuracy.

Examples of grass-reference evaporation and of evapotranspiration after Penman-Monteith are displayed in Fig. 4. Firstly, the main influence on evaporation clearly is due to the influence of clouds on the surface net radiation (reduced available energy). Secondly, the landuse classification is important for the fraction of net radiation to the evaporation rate. Furthermore, the difference between the land and sea surface can easily be seen. The left panel in Fig. 4 illustrates a first estimate of the spatial variability of an evaporation for grass and can be used as a first calibration of other measurements. The right one shows much larger evaporation rates in southern Scandinavia, depending on the classified forests, whereas in Poland and Germany the forested areas are underestimated using the USGS landuse classification which leads to a significant reduction of evapotranspiration in this area. In both figures, longitudinal and latitudinal cross-sections are plotted to demonstrate the variabilities in longitude as well as in latitude.

Figure 5 is a comparison of satellite-inferred with surface-measured energy flux densities for the anchorstation Tharandter Wald, located south-east of Dresden, Saxony, Germany. The left panel shows a distinct diurnal cycle of net radiation for typical clear-sky conditions. A good agreement between the ground based measurements and the satellite inferred net radiation has been achieved. As for the other energy flux densities, potential evaporation after Priestley-Taylor has led to the highest evaporation rates and was always larger than the measured evaporation. The grass-reference and the actual evaporation after Penman-Monteith estimated from satellite data are close to the surface measured evaporation with an uncertainty of about  $\pm 50 \text{ W m}^{-2}$ . Big differences can be seen in the soil heat fluxes, where the satellite inferred flux density is absolutely overestimated. This is due to an insufficient USGS landuse classification. In this data set the surroundings of the anchorstation Tharandter Wald are classified as grass land, whereas in reality this is a  $60 \text{ km}^2$  forested area. The large overestimation of the soil heat flux leads to a large underestimation of sensible heat

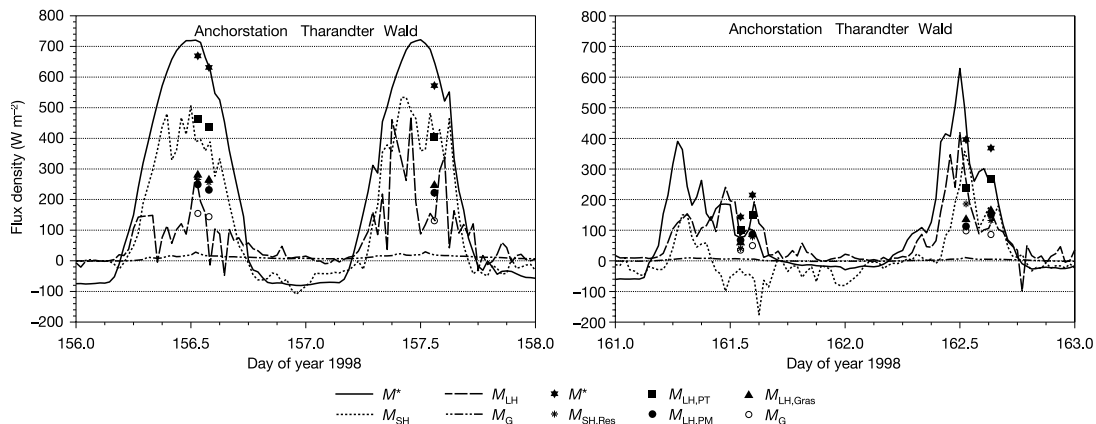


**Fig. 5.** Energy flux densities, measured at anchorstation Tharandter Wald (solid lines) and inferred from NOAA-AVHRR Data (symbols) for four different days in 1998.

flux, which is computed as the residuum of the energy balance equation (Eq. 1).

The right panel in Fig. 5 shows the same intercomparison, but for cloudy days at the anchorstation Tharandter Wald. Here clouds reduce net radiation and, subsequently, all energy flux densities. In this period negative flux densities have also been measured at surface during the day, whereas only positive fluxes can be inferred from the satellite measurements, due to the relation to positive net radiation. Counter-gradient fluxes occurring mainly during wintertime in forested areas cannot be currently estimated from space using passive meteorological satellite data.

## Summary and outlook

The satellite data analysis scheme SESAT was developed to study the energy and water cycle at different spatial and temporal scales and was applied to passive remotely sensed data. SESAT consists of several modules to compute cloud properties, surface properties, surface radiant and energy flux densities. Using SESAT, a first estimate of surface energy flux densities may be inferred. It has been shown that most of the parameters needed for the computation can be derived from meteorological satellite data. The information about the atmospheric boundary layer properties has to be based on ground based observations, where the relative humidity field

can be spatially interpolated. For wind speed, more detailed simulations applying mesoscale models have to be carried out to consider the influence and dependence on heterogeneous terrain.

Comparisons of the radiation, inferred from satellite data and measured at surface, show sufficient accuracy, whereas for the energy flux densities more observations are necessary. For the soil heat flux, including the storage within the canopy, more landuse types will be investigated to develop empirical net radiation/NDVI relationships and the temporal temperature variation from future MSG data will be used to derive soil moisture. For the latent heat flux densities, different model simulations will be carried out to get a better fractioning of the flux densities depending on landuse types. To improve the accuracy of sensible heat flux densities, more detailed information about the vertical temperature profile, especially in the atmospheric boundary layer, is needed, which may be realised within future satellite missions. However, by applying SESAT to passive remotely sensed data a first estimate of surface energy flux densities was inferred. These results strongly depend on net radiation as well as on the applied landuse classification. A detailed and accurate landuse classification will allow a more accurate estimation of energy flux densities.

*Acknowledgments:* The author would like to thank the two anonymous reviewers for their valuable comments.

## References

- Avisar R. & Schmidt T. 1998. An evaluation of the scale at which ground-surface heat flux patchiness affects the convective boundary layer using large-eddy simulations. *J. Atmos. Sci.* 55: 2666–2689.
- BAHC Core Project Office 1993. *Biospheric aspects of the hydrological cycle — the operational plan*. Report No. 27, IGBP — Global Change, 103 pp.
- Berger F.H. 2001. *Bestimmung des Energiehaushalts am Erdboden mit Hilfe von Satellitendaten*. Tharandter Klimaprotokoll, Band 5, 206 pp.
- Berger F.H. 1995. Inference of the climatic efficiency of clouds from satellite measurements. *Int. J. Remote Sensing* 16: 2903–2926.
- Berger F.H. 1992. *Die Bestimmung des Einflusses von hohen Wolken auf das Strahlungsfeld und auf das Klima durch Analyse von NOAA-AVHRR Daten*, Bd. Serie A Monographien von Band 6, Heft 3. Meteorologische Abhandlungen des Instituts für Meteorologie der Freien Universität Berlin, Verlag Dietrich Reimer, 110 pp.
- Berger F.H., Stuhlmann R. & Jagdhuhn S. 1995. Radiation budget components inferred from satellite data for the Baltic Sea. In: *The Meteorological Satellite Data User's Conference, Winchester, UK, 4–8 September 1995*, 417–425, Eumetsat.
- Berger M. 1997. *Flächenmittel der Energieflüsse in einem semi-ariden Testgebiet*. Geowissenschaften, Shaker Verlag, 164 pp.
- Brutsaert W. 1988. *Evaporation into the atmosphere; theory, history and applications*. D. Reidel Publishing Comp., Dordrecht, 299 pp.
- Chahine M.T. 1992. The hydrological cycle and its influence on climate. *Nature* 359: 373–380.
- Derrien M., Farki B., Harang L., Legleau H., Noyalet A., Pochic D. & Sairouni A. 1993. Automatic cloud detection applied to NOAA-11/AVHRR imagery. *Rem. Sens. Environ.* 46: 246–267.
- de Rooy W.C. & Holtslag A.A.M. 1999. Estimation of surface radiation and energy flux densities from single-level weather data. *J. Appl. Meteor.* 38: 526–540.
- DVWK 1996. *Ermittlung der Verdunstung von Land- und Wasserflächen. Merkblätter 238*, Deutscher Verband für Wasserwirtschaft und Kulturbau e.V., 135 pp.
- Friedl M.A. 1996. Relationships among remotely sensed data, surface energy balance, and area-averaged fluxes over partially vegetated land surfaces. *J. Appl. Meteor.* 35: 2091–2103.
- Gao W., Coulter R.L., Lesht B.M., Qiu J. & Wesely M.L. 1998. Estimating clear-sky regional surface fluxes in the southern great plains atmospheric radiation measurement site with ground measurements and satellite observations. *J. Appl. Meteor.* 37: 5–22.
- Hagemann S. 1999. *Derivation of global GCM boundary conditions from 1 km land use satellite data*. Techn. Ber. No. 289, Max-Planck-Institut für Meteorologie, 34 pp.
- Khattak S., Vaughan R.A. & Cracknell A.P. 1991. Sun glint and its observation in AVHRR data. *Rem. Sens. Environ.* 37: 101–116.
- Key J.R. 1999. *Streamer — user's guide*. Technical Report 96-01, Department of Geography, Boston University, 108 pp.
- Koslowsky D. 1977. Digitale Bearbeitung der am Meteorologischen Institut der FU empfangenen Scanning-Radiometer (SR) — Daten der NOAA — Wetter-satelliten. Teil IV: Geographische Entzerrung und Darstellung in stereographischer Landkartenprojektion. *Beilage zur Berliner Wetterkarte des Institutes für Meteorologie der Freien Universität Berlin*, 32 pp.
- Koslowsky D. 1997. Signal degradation of the AVHRR shortwave channels of NOAA 11 and NOAA 14 by daily monitoring of desert targets. *Adv. Space Res.* 19: 1355–1358.
- Mason P.J. 1994. Large-eddy: A critical review of the technique. *Q. J. R. Meteorol. Soc.* 120: 1–26.
- Maidment D.R. 1993. *Handbook of hydrology*. McGraw-Hill, Inc. 1424 pp.
- Mausser W. & Schädlich S. 1998. Modeling the spatial distribution of evapotranspiration on different scale using remote sensing data. *J. Hydrol.* 212–213: 251–267.
- Mecklenburg S., Berger F.H. & Bernhofer C. 1999. The influence of cloud optical thickness on terrestrial long-wave radiation of a spruce forest for different cloud types. *Z. Meteor.* 8: 22–27.
- Moeng C.-H., Cotton W.R., Bretherton C., Chlond A., Khairoutdinov M., Krueger S., Lewellen W.S., MacVean M.K., Pasquier J.R.M., Rand H.A., Siebesma A.P., Stevens B. & Sykes R.I. 1996. Simulation of a stratocumulus-topped planetary boundary layer: Intercomparison among different numerical codes. *Bull. Amer. Meteor. Soc.* 77: 261–278.
- Monteith J.L. 1965. Evaporation and environment. In: Fogg E.G. (ed.), *The state and movement of water in living organisms*, Cambridge University Press, pp. 205–234.
- Moreno J.F. & Green R.O. 1996. Surface and atmospheric parameters retrieval from AVIRIS data: The importance of non-linear effects. In: *Summaries of the Sixth Annual JPL Airborne Geoscience Workshop, March 4–8, 1996*. 9 pp.
- Nakajima T. & King M.D. 1990. Determination of the optical thickness and effective particle radius of clouds from reflected solar radiation measurements. Part I: Theory. *J. Atmos. Sci.* 45: 1878–1893.
- Nemani R.R. & Running S.W. 1989. Testing a theoretical climate-soil-leaf area hydrological equilibrium of forests using satellite data and ecosystem simulation. *Agric. Forest Meteorol.* 44: 245–260.
- Podlasly C. & Berger F.H. 2001. Ableitung von UV-Strahlungsflüssen am Erdboden für den Juli und August 1998 (BERLIOZ). *DACH-MT Tagung, Wien/Österreich, Österreichische Beiträge zu Meteorologie und Geophysik*, Heft 27, Publ. Nr. 399, 12 pp.
- Priestley C.H.B. & Taylor R.J. 1972. On the assessment of surface heat flux and evapotranspiration using large-scale parameters. *Mon. Weather Rev.* 100: 81–92.
- Raschke E. 1994. *Scientific plan for the Baltic Sea Experiment (BALTEX)*, 2nd ed. 84 pp.
- Schwiebus A. & Podlasly C. 2001. Bestimmung des Bodenwärmestromes für unterschiedliche Oberflächen in Abhängigkeit vom normalisierten Differenzenvegetati

- onsindex NDVI. *DACH-MT Tagung, Wien/Österreich, Österreichische Beiträge zu Meteorologie und Geophysik*, Heft 27, Publ. Nr. 399, 7p.
- Vermote E., Tanre D., Deuze J.L., Herman M. & Morcrette J.J. 1995. *Second simulation of the satellite signal in the solar spectrum (6S)-6S user guide*. Techn. Ber., NASA Goddard Space Flight Center, 216 pp.
- Wierenga J. 1993. Representative roughness parameters for homogeneous terrain. *Boundary-Layer Met.* 63: 323–363.
- WMO 1990. *Scientific plan for the global energy and water cycle experiment*. Techn. Ber. WCRP-40, WMO/TD-No. 376, International Council of Scientific Unions and World Meteorological Organization, 83 pp.

*Received 23 January 2002, accepted 11 October 2002*